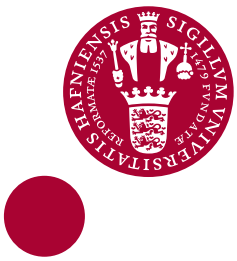

Bragg coherent x-ray diffractive imaging of a single indium phosphide nanowire

Dzhigaev, D.; Shabalin, A.; Stankevic, T.; Lorenz, U.; Kurta, R. P.; Seiboth, F.; Wallentin, J.; Singer, A.; Lazarev, S.; Yefanov, O. M.; Borgstrom, M.; Strikhanov, M. N.; Samuelson, L.; Falkenberg, G.; Schroer, C. G.; Mikkelsen, A.; Feidenhans'l, R.; Vartanyants, I. A.

Published in:
Journal of Optics

DOI:
10.1088/2040-8978/18/6/064007

Publication date:
2016

Document version
Publisher's PDF, also known as Version of record

Bragg coherent x-ray diffractive imaging of a single indium phosphide nanowire

2016 J. Opt. 18 064007

(http://iopscience.iop.org/2040-8986/18/6/064007)

OPEN ACCESS
IOP Publishing
Journal of Optics
J. Opt. **18** (2016) 064007 (10pp)
doi:10.1088/2040-8978/18/6/064007

Bragg coherent x-ray diffractive imaging of a single indium phosphide nanowire

D Dzhigaev[1,2], A Shabalin[1], T Stankevič[3], U Lorenz[4], R P Kurta[5], F Seiboth[6], J Wallentin[7], A Singer[8], S Lazarev[1,9], O M Yefanov[10], M Borgström[11], M N Strikhanov[1], L Samuelson[11], G Falkenberg[1], C G Schroer[1,12], A Mikkelsen[11], R Feidenhans'l[3] and I A Vartanyants[1,2]

[1] Deutsches Elektronen-Synchrotron DESY, Notkestraße 85, D-22607 Hamburg, Germany
[2] National Research Nuclear University, 'MEPhI', 115409 Moscow, Russia
[3] Niels Bohr Institute, University of Copenhagen, DK-2100 Copenhagen, Denmark
[4] Institut für Chemie, Universität Potsdam, Karl-Liebknecht-Strae 24-25, D-14476 Potsdam, Germany
[5] European XFEL GmbH, Albert-Einstein-Ring 19, D-22761, Hamburg, Germany
[6] Institute of Structural Physics, Technische Universität Dresden, D-01062 Dresden, Germany
[7] Synchrotron Radiation Research, Lund University, SE-22100 Lund, Sweden
[8] Department of Physics, University of California, San Diego, La Jolla, CA 92093, USA
[9] National Research Tomsk Polytechnic University (TPU), pr. Lenina 30, 634050 Tomsk, Russia
[10] Center for Free-Electron Laser Science CFEL, Notkestraße 85, D-22607 Hamburg, Germany
[11] Solid State Physics, Lund University, SE-22100 Lund, Sweden
[12] Department Physik, Universität Hamburg, Luruper Chaussee 149, D-22761 Hamburg, Germany

E-mail: Ivan.Vartaniants@desy.de

Received 17 December 2015, revised 4 March 2016
Accepted for publication 30 March 2016
Published 6 May 2016

Abstract

Three-dimensional (3D) Bragg coherent x-ray diffractive imaging (CXDI) with a nanofocused beam was applied to quantitatively map the internal strain field of a single indium phosphide nanowire. The quantitative values of the strain were obtained by pre-characterization of the beam profile with transmission ptychography on a test sample. Our measurements revealed the 3D strain distribution in a region of 150 nm below the catalyst Au particle. We observed a slight gradient of the strain in the range of $\pm 0.6\%$ along the [111] growth direction of the nanowire. We also determined the spatial resolution in our measurements to be about 10 nm in the direction perpendicular to the facets of the nanowire. The CXDI measurements were compared with the finite element method simulations and show a good agreement with our experimental results. The proposed approach can become an effective tool for *in operando* studies of the nanowires.

S Online supplementary data available from stacks.iop.org/jopt/18/064007/mmedia

Keywords: Bragg coherent x-ray diffractive imaging, InP nanowires, strain field

(Some figures may appear in colour only in the online journal)

1. Introduction

Free standing semiconductor nanowires (NWs) have been broadly studied during the past decade due to their unique mechanical, electronic, and optical properties. Numerous applications based on NWs have been demonstrated in photonics [1–3], photovoltaics [4, 5], electronics [6, 7], and other fields [8].

NWs are commonly fabricated via gold (Au) metal particle-assisted epitaxial growth [9]. The wire grows under the Au particle, thus lifting it up. It is well known that the Au particle influences the wire dimensions during the growth, for example by determining the wire diameter. However, to our

best knowledge, the influence of a catalyst particle on the three-dimensional (3D) strain inside the wire has not been discussed so far. This aspect is of great interest because the presence of strain and defects may alter the properties of NWs. In semiconductors, the band gap and charge carrier mobility depend significantly on the strain state [10, 11].

A number of comprehensive characterization tools, such as high- resolution electron microscopy [12, 13], Raman spectroscopy [14] and various x-ray techniques can be used to probe the physical, chemical, and electronic properties of NWs. High penetration depth of x-rays, comparing to electrons, for example, allows structural characterization of thick samples on the nanoscale without destructive sample preparation [15, 16]. Modern third generation synchrotron radiation facilities (see, for example, [17]) are well-suited x-ray sources for NW structure characterization. They generate stable, bright, and coherent x-ray beams, which can be focused below 100 nm [18–20]. That gives an opportunity to image the inner structure of a single NW using the following techniques. Scanning x-ray diffraction mapping gives information about strain both for ensembles of NWs and for single nano-objects [21], however, the resolution is limited by the beam size [22–24]. Coherent x-ray diffractive imaging (CXDI) provides local information about the shape and strain of the NW in 2D and 3D with high spatial resolution [25].

In the Bragg CXDI technique [26–28] an isolated object is illuminated by a coherent x-ray beam producing the diffraction pattern on a 2D detector in the far-field. The 3D reciprocal space map is constructed from a series of such 2D images taken at different angular positions in the vicinity of the Bragg angle. Phase retrieval algorithms [29] reconstruct the 3D shape function and strain distribution in a crystalline sample.

In our previous study, Bragg CXDI nano-diffraction measurements were successfully performed to study the structure of a single 100 nm GaAs NW [30]. However, due to experimental challenges it was not possible to reconstruct the structure of the NW with conventional phase retrieval methods. A high-resolution reconstruction of a 2D cross-section of a single InAs NW was obtained earlier [31]. However, in this work, an assumption of a flat wavefront at the position of the sample was applied. In our present work the reconstruction of the 3D strain field inside a single InP NW was obtained. The result is corrected by the probe function reconstructed from ptychographical measurements. The study was focused on the NW part close to the Au catalyst particle. In this region of the NW, the maximum of the strain variations is expected due to the relaxation of lattice mismatch strain between InP and Au.

2. Theory

In the following, we describe a theoretical basis of the 3D strain field reconstruction using Bragg CXDI. The scheme of the experimental geometry is shown in figure 1(a). A right-hand coordinate system x, y, z that is used in the discussion is oriented in such a way that the positive z axis direction is aligned with the NW growth direction and the $\mathbf{H}_{111}$ reciprocal lattice vector. Axis y is oriented perpendicular to the scattering plane.

A reciprocal space coordinate system Q_x, Q_y, Q_z is oriented according to the real space coordinates. The scheme of Bragg scattering geometry in reciprocal space is presented in figure 1(b). Rotation of the sample around y axis by a small angle $\Delta\omega$ leads to the shift of the cross section in reciprocal space by the same transformation of rotation. The position of the central point of the detector in reciprocal space in small angle approximation is shifted by $\Delta\mathbf{Q}_x$ along the Q_x axis (see figure 1(b)).

An amplitude of the scattered wave satisfying the Bragg condition for the strained crystal in the kinematical approximation can be represented as [28, 32]

$$A(\mathbf{Q}) = \int S(\mathbf{r}) E_{\text{in}}(\mathbf{r}) \mathrm{e}^{-\mathrm{i}\mathbf{Q}\cdot\mathbf{r}} \mathrm{d}\mathbf{r}, \tag{1}$$

where

$$S(\mathbf{r}) = s(\mathbf{r}) \mathrm{e}^{-\mathrm{i}\mathbf{H}\cdot\mathbf{u}(\mathbf{r})}. \tag{2}$$

Here $\mathbf{r}$ and $\mathbf{Q}$ are real and reciprocal space coordinates respectively, $S(\mathbf{r})$ is the complex object function consisting of the shape function $s(\mathbf{r})$ and the phase, determined by the displacement field $\mathbf{u}(r)$, $\mathbf{H}$ is the reciprocal lattice vector, and $E_{\text{in}}(\mathbf{r})$ is an incident wavefield. The CXDI measurement comprises a collection of the diffraction patterns in the detector plane for a range of angular positions ω of the sample around y axis. The step of rotation is chosen by the sampling condition in the Q_x direction. In other words, the distance between the two neighboring diffraction patterns in reciprocal space $\Delta\mathbf{Q}_x$ along the Q_x direction must be small enough to satisfy the Shannon sampling condition π/D_x, where D_x is the dimension of the scattering object in real space along the x axis. From the geometry shown in figure 1 it follows that

$$|\Delta\mathbf{Q}_x| = |\mathbf{H}_{111}|\Delta\omega. \tag{3}$$

Taking into account that $|\mathbf{H}_{111}| = 4\pi \sin(\theta_{\text{B}})/\lambda$, the sampling condition for a step of rotation can be expressed as

$$\Delta\omega < \frac{\lambda}{4D_x \sin(\theta_{\text{B}})}. \tag{4}$$

Further, the measured set of diffraction patterns is combined into a 3D intensity distribution in reciprocal space $I(\mathbf{Q}) = |A(\mathbf{Q})|^2$. After applying the phase retrieval procedure, according to equation (1) the function

$$\widetilde{S}(\mathbf{r}) = S(\mathbf{r}) E_{\text{in}}(\mathbf{r}), \tag{5}$$

is reconstructed.

The 2D distribution of the incoming wavefield $E_{\text{in}}(\mathbf{r})$ at the sample position is determined using x-ray ptychography on a test sample. This 2D distribution can be propagated forward and backward in order to obtain the 3D distribution of the incoming wavefield $E(\mathbf{r})$ in the region of the sample. Using the knowledge of $E_{\text{in}}(\mathbf{r})$ the 3D real space image $S(\mathbf{r})$ of the sample can be deduced by applying equation (5). According to equation (2), the phase of $S(\mathbf{r})$ is $\varphi(\mathbf{r}) = -\mathbf{H}\cdot\mathbf{u}(\mathbf{r})$.

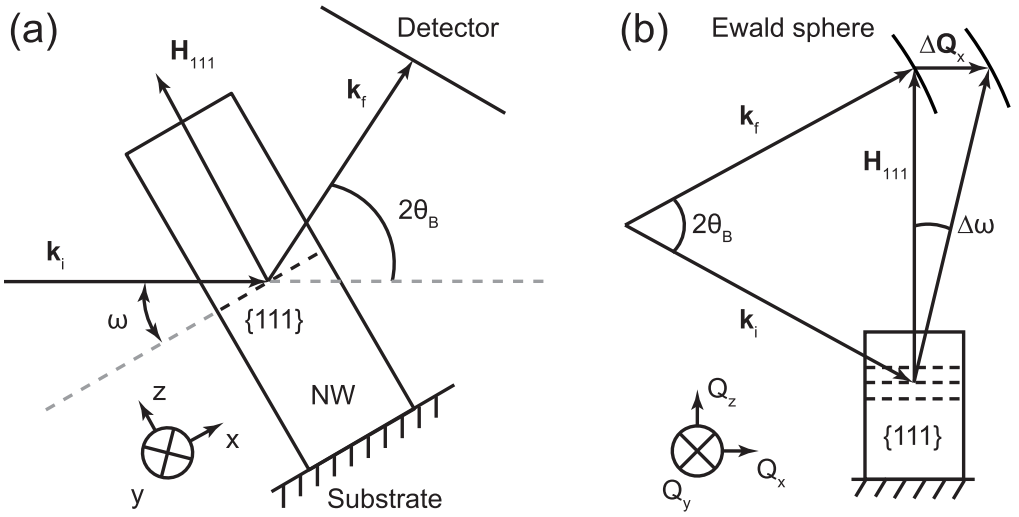

Figure 1. Scheme of the scattering geometry. (a) Real space scheme. An incident x-ray beam with the wave vector $\mathbf{k}_i$ is diffracted at the Bragg angle θ_B with the wave vector $\mathbf{k}_f$ with respect to {111} InP crystalline planes. $\mathbf{H}_{111}$ is a reciprocal lattice vector and ω is a variable angle during the rocking curve scan. (b) Reciprocal space scheme. The part of the Ewald sphere constructed on $\mathbf{k}_i$ and $\mathbf{k}_f$ vectors represents the measured cross section in reciprocal space. The angular step of rotation during the rocking curve scan is denoted by $\Delta\omega$.

By measuring several Bragg reflections, different strain components can be determined using the following relation with the displacement field

$$\varepsilon_{ij} = \frac{1}{2}\left(\frac{\partial u_j}{\partial x_i} + \frac{\partial u_i}{\partial x_j}\right). \tag{6}$$

In our experiment measurements were performed around a single Bragg peak, therefore the reconstructed phase contains the information about the projection of the displacement field along the reciprocal lattice vector $\mathbf{H}$. According to introduced coordinate system (see figure 1) one gets the phase $\varphi(\mathbf{r}) = -|\mathbf{H}| \cdot u_z(\mathbf{r})$.

By applying equation (6), we can determine the $\varepsilon_{zz}(\mathbf{r})$ component of the strain field

$$\varepsilon_{zz}(\mathbf{r}) = \frac{\partial u_z(\mathbf{r})}{\partial z} = -\frac{1}{|\mathbf{H}|}\frac{\partial \varphi(\mathbf{r})}{\partial z}. \tag{7}$$

These values give a measure of the strain field along the growth direction of the NW.

3. Sample description

InP NWs were grown in a low-pressure (100 mbar) metal organic vapor phase epitaxy (MOVPE) system with a total flow of 6 l min^{-1} using hydrogen as carrier gas. The seed particles were 80 nm gold aerosols [33] at a density of 0.2 μm^{-2}, deposited on an InP (111) substrate. The growth precursors were phosphine (PH_3), molar fraction $\chi_{PH_3} = 6.3 \times 10^{-3}$ and trimethylindium (TMI) $\chi_{TMI} = 1.2 \times 10^{-5}$. Hydrogen chloride (HCl), $\chi_{HCl} = 8.3 \times 10^{-6}$ was used to control the radial growth. To desorb surface oxides, the samples were first annealed at 550 °C for 10 min under a PH_3/H_2 gas mixture. The reactor was then cooled to $T_G = 420$ °C, at which temperature InP NW growth was initiated by adding TMI. At this temperature the Au–In alloy particle is liquid. After 15 s of nucleation time, HCl was added. After 15 min, TMI and HCl were switched off and the sample was cooled under PH_3/H_2. At the temperature about 320 °C the Au–In particle solidifies. The typical structure for the InP NWs is a mixture of zinc-blende (ZB) and wurtzite (WZ) phases [34]. These two structures have slightly different lattice parameters considering the geometrical conversion in [111] direction. The dimensions of the NW in our sample were about 100 nm in diameter and 7.5 μm in length and the average separation between single wires was 2.5 μm. For CXDI experiments the substrate was cracked into parts to get a sharp corner with a single NW at the edge. Scanning electron microscopy (SEM) images of the sample are shown in figure 2.

4. Experiment

The experiment on a single free standing InP NW was performed at the nanoprobe endstation [35] of the P06 beamline at the PETRA III synchrotron radiation source at DESY (Hamburg, Germany). The geometry of the experiment is shown in figure 3(a). Vertical (V) and horizontal (H) nano-focusing lenses (NFLs) were used to focus the incident x-ray beam with 15.25 keV photon energy. For our set of NFLs the focal distance was 26.33 mm (V) by 16.66 mm (H) with a depth of focus of 184 μm (V) by 107 μm (H). The incoming photon flux of the beam was 4×10^7 photons s^{-1}. A 2D hybrid-pixel detector Pilatus 300 K (Dectris, Switzerland) with a pixel size of 172 × 172 μm^2 was used to record the diffraction patterns in the far-field regime.

As it follows from the theory, knowledge of the illumination function (probe) at the sample position is essential for the reliable reconstruction of the object (see equation (5)). To obtain this information, a tantalum (Ta) resolution chart in the form of a Siemens star, fabricated by nano-lithography, was

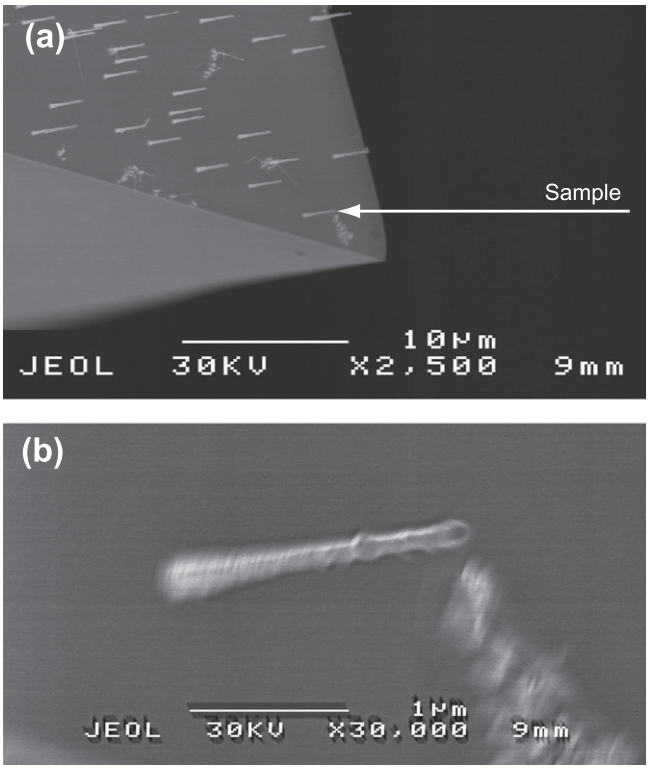

Figure 2. Sample studied in the experiment. (a) SEM image of the forest of InP NWs. The arrow points to the investigated NW on the substrate. (b) SEM image of the investigated InP NW after the experiment. The substrate is tilted by 12° with respect to the view direction.

used. It was positioned close to the focal plane of the beam. A ptychographical measurement was performed with the detector placed 2.2 m downstream in transmission geometry. A 2D reconstruction of the wavefield was obtained in the object plane (see figure 3(b)). Afterwards, a numerical propagation of this 2D function was used to obtain a 3D distribution of the wavefield $E_{\mathrm{in}}(\mathbf{r})$ (see figures 3(c) and (d)). The focal plane position was determined by the sharpness criterion [36]. In our case it is calculated as the maximum value of the integral $F(w) = \int I_{\mathrm{in}}^2(u, v, w)\mathrm{d}u\mathrm{d}v$ as a function of w, where $I_{\mathrm{in}}(u, v, w)$ is the incident beam intensity, u, v are coordinates in transverse direction, and w is the coordinate along the beam. Our reconstruction revealed an x-ray beam focus size of 70 ± 0.3 nm (V) by 91.4 ± 1.1 nm (H) at full width at half maximum (FWHM) [37]. In order to place the sample into the focus of the beam the following procedure was implemented. After reconstruction of the beam profile the Siemens star was positioned at the focal plane. An in-line optical microscope was focused on the test pattern and afterwards, the NW sample was brought in the same position with a precision better than 10 μm.

For the CXDI measurements on the NW, the detector was positioned 2.3 m downstream from the sample in Bragg scattering geometry. The Bragg angle was $\theta_{\mathrm{B}} = 6.89°$ for the 111 InP reflection at the given energy. The substrate was mounted vertically providing a horizontal orientation of the NW and a possibility to measure the selected reflection in the horizontal diffraction plane (see figure 3(a)). A fluorescence detector was positioned close to the sample and perpendicular to the beam. It was used to locate a single wire in the array by mapping the combined signal from In, P and Au. An isolated free-standing NW at the corner of the substrate (see figure 2(a)) was selected for the CXDI measurements. We want to note that the beam profile (amplitude and phase) is almost constant on the size of the NW in the region close to the focus (see insets in figures 3(c) and (d)).

The 2D fluorescence mapping in the region close to the Au particle with a step size of 50 nm was performed to locate the position of the x-ray beam on the NW. The CXDI measurements were performed 150 nm below the Au particle position. In total 31 diffraction patterns were measured in the angular range of ±1° with an increment of $\Delta\omega = 0.065°$ around the Bragg peak. For a NW with the diameter D = 100 nm and the experimental conditions considered in this work, the sampling condition (see equation (4)) gives the value for the angular step of $\Delta\omega < 0.097°$. The acquisition time was 400 s per frame. An example of recorded diffraction pattern at a central angular position is shown in figure 4(a).

5. Results and discussion

The full 3D scattered intensity distribution around the 111 InP Bragg peak (see figure 4(b)) was obtained by combining the 2D intensity distributions measured at different angular positions around this peak. Measured 2D scattering intensities were interpolated on a uniform rectangular grid with a set of basis vectors along the Q_x, Q_y, and Q_z directions. To minimize the error of the interpolation (i.e. to have sufficient sampling of the measured data) the size of the grid voxel in reciprocal space was chosen to be equal to one of the detector pixel (0.0058 nm^{-1}). It is several times smaller than the distance between neighboring measured 2D diffraction patterns along the Q_x direction (0.021 nm^{-1}).

The resulting 3D reciprocal space map reveals a symmetric hexagonal orientation of streaks with finely resolved fringes (see figure 4(b)). They arise from x-ray scattering on the side facets of the NW and reflect its hexagonal cross-section. For the CXDI reconstruction, we first considered the central slice ($Q_z = 0$) through the 3D intensity distribution around the Bragg peak. Using the combination of hybrid input–output and error-reduction algorithms [29] a 2D projection of the complex-valued object function in the x–y plane was reconstructed. The reconstruction started with a loose round-shaped support which was several times updated during the phase retrieval procedure by applying Shrinkwrap method [38]. The initial guess was set to be random both for the amplitude and phase within the support region. The resulted 2D reconstruction was used to determine a tight support for a set of phase retrieval runs for the full 3D dataset. In order to ensure the reliability of results, 30 successful reconstructions with the least error metrics were selected and averaged. Complex conjugate solutions were separated in the averaging procedure.

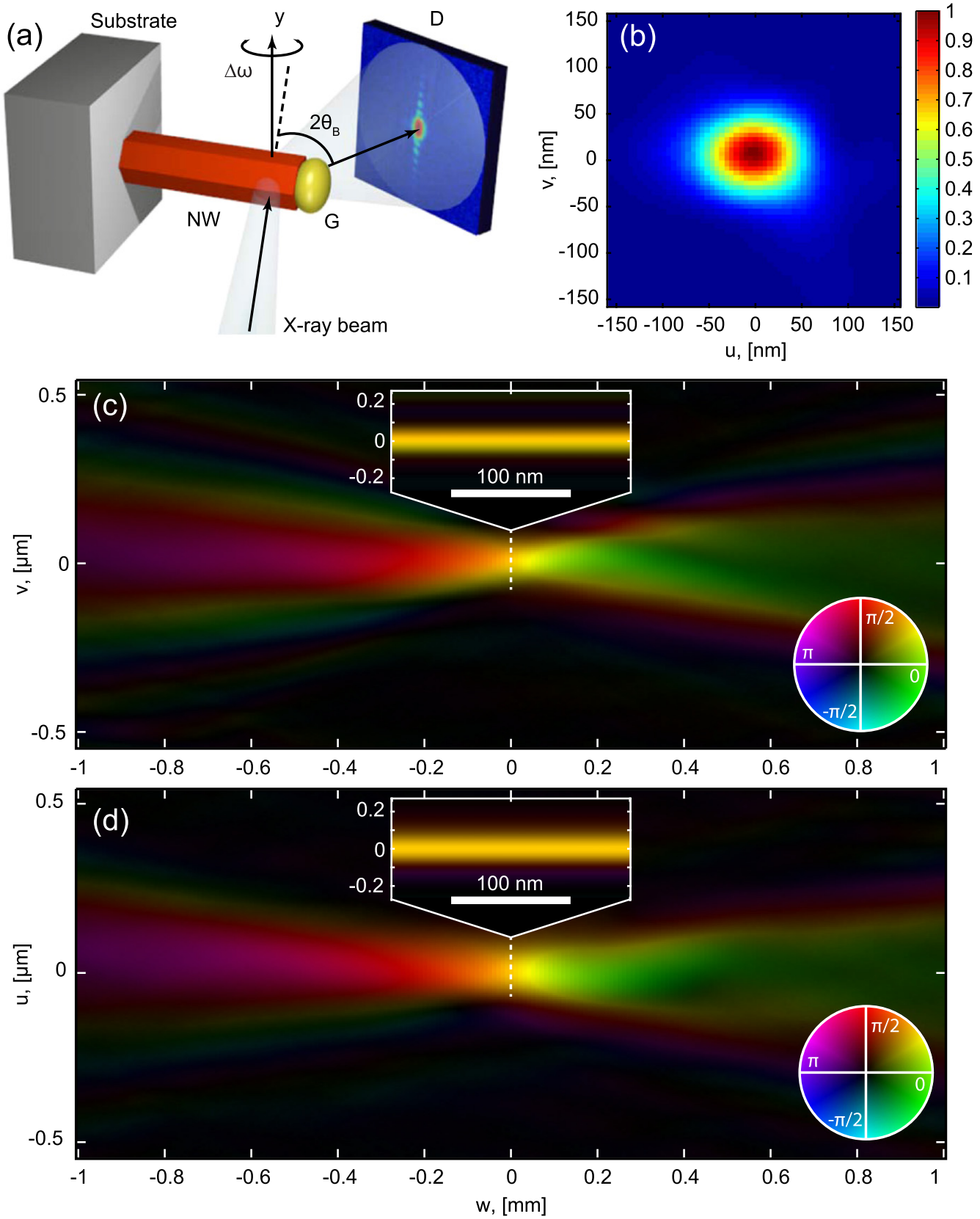

Figure 3. Experimental setup and wavefield reconstruction. (a) A single NW with a gold particle (G) on the top was mounted on a moving stage. The 2D detector (D) was placed downstream to measure the 111 Bragg peak at $2\theta_B = 13.78°$ degrees relative to the optical axis of the incident x-ray beam. The angular scan was performed around the y axis. (b) Intensity of the focused beam, reconstructed at the sample plane from ptychography measurements. (c) and (d) Distribution of the wavefield obtained by numerical propagation. Insets represent 100 nm region around sample position in the beam. Brightness corresponds to the normalized amplitude and color to the phase.

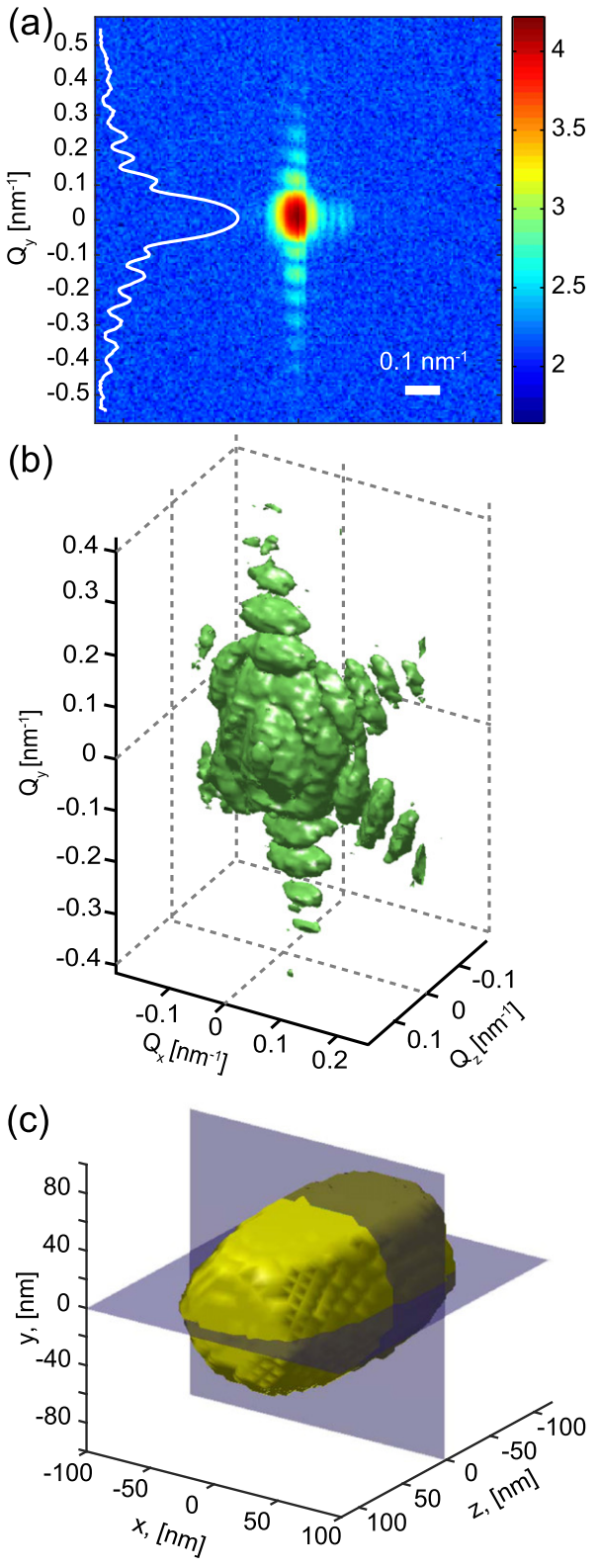

Figure 4. Measured data and the reconstructed 3D object. (a) An example of a single 2D diffraction pattern within the measured dataset (logarithmic scale). The profile plot represents the vertical slice of intensity through the center of the Bragg peak (logarithmic scale). (b) Isosurface of the 3D intensity distribution in the vicinity of the InP 111 Bragg peak. (c) Isosurface of the reconstructed shape function $s(\mathbf{r})$. Cross-sectional profiles are taken in the planes $y = 0$ and $z = 0$ (see figure 5).

In order to correct for the contribution of the illumination function $E_{\text{in}}(\mathbf{r})$ (see equation (5)), the reconstructed 3D object was divided by the 3D complex illumination function, obtained from the ptychographical reconstruction (see figure 3(b)). By this procedure we obtained the 3D distribution of the complex-valued function $S(\mathbf{r})$ and it was an important step in obtaining quantitative and reliable information about the strain distribution in the NW. Reconstructed real space functions were interpolated on a ten times finer grid to improve the visual representation of the results. A final image of the reconstructed 3D shape function is presented in figure 4(c). The diameter of the reconstructed NW was determined to be 90 nm from edge to edge and the length determined by the size of the probe was 160 nm. These values are in a good agreement with the SEM measurements.

The amplitude, phase, and $\varepsilon_{zz}(\mathbf{r})$ strain profiles of the NW in the planes corresponding to $y = 0$ and $z = 0$ are presented in figure 5. The hexagonal shape of the NW was obtained as expected from the symmetry of the 3D diffraction intensity distribution (see figure 5(a)). A 2D slice of the amplitude at $y = 0$ (see figure 5(b)) shows the decay in the region of the positive z-axis direction. That effect can be attributed to the influence of the catalyst particle on crystal lattice regularity in the region close to the interface between InP and Au.

A threshold of 30% of the amplitude shown in figures 5(a) and (b) was considered as a region of interest within the NW. Results of the phase and strain reconstruction in this region are shown in figures 5(c)–(f). It can be seen that the phase $\varphi(\mathbf{r})$ values vary in the range from -0.8 to 1.2 rad with clearly visible asymmetry with respect to the vertical central axis of the NW. The $\varepsilon_{zz}(\mathbf{r})$ strain distribution was obtained using equation (7) by gradient evaluation in 3D along z. The values of strain component $\varepsilon_{zz}(\mathbf{r})$ vary in the range from -0.6% to 0.6%. The maximum positive strain values were observed at the edges of the NW, which could be an indication of the surface induced stress (see figure 5(e)). The variation of the strain values in the x–y plane are within $\pm 0.1\%$. From the slices at $y = 0$ (see figures 5(d) and (f)) a slight gradient of the phase and rise of the strain values are visible in the positive z direction. This effect can be explained as a result of a lattice strain relaxation at the boundary between InP and Au particle. Close to the interface, the unit cell of the NW shrinks laterally due to the smaller lattice parameter of Au and stretches along the z direction because of the Poisson effect. As a consequence of the NW lattice relaxation, a positive strain $\varepsilon_{zz}(\mathbf{r}) > 0$ below the Au particle is induced (see figure 5(f)).

We first obtained a rough estimate of the achieved resolution by the extent of the intensity signal in reciprocal space. For a signal at $|\mathbf{Q}_{y,\max}| = 0.46\,\text{nm}^{-1}$ reached in our experiment (see intensity scan in figure 4(a)) the spatial resolution was 13.5 nm in the direction perpendicular to facets of the NW. The extent of the signal along the NW was $|\mathbf{Q}_{z,\max}| = 0.23\,\text{nm}^{-1}$, which gives a limitation of the resolution down to 27 nm. We next focused more closely on the resolution of the reconstruction perpendicular to the facets of the NW. It was evaluated in real space by the edge response.

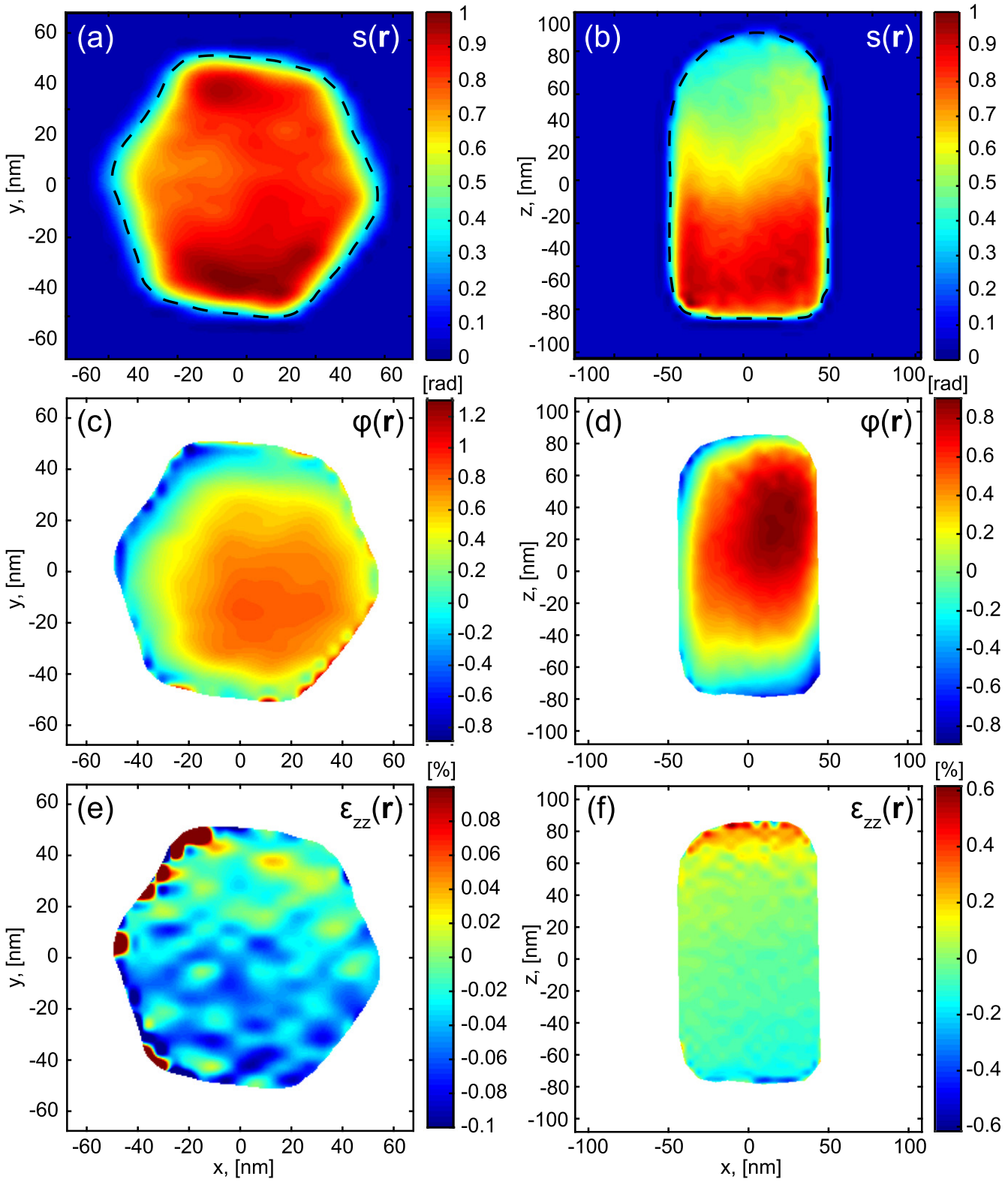

Figure 5. Result of Bragg CXDI reconstruction represented as plane slices from figure 4(c). (a) and (b) are normalized amplitudes of the reconstructed part of the NW. The dashed line truncate the region of the reconstruction shown in (c)–(f) at the level of 30%. (c) and (d) 2D slices of the phase distribution $\varphi(\mathbf{r})$. (e) and (f) 2D slices of the $\varepsilon_{zz}(\mathbf{r})$ strain distribution.

Six scans were performed in the direction normal to every facet of the NW and their profiles were averaged (see figure 6(a)). The resulting profile was fitted by the error function. The line spread function (LSF) was obtained by taking the derivative of the fitted profile (see figure 6(b)). The FWHM of the LSF resulted in a resolution of 10 nm.

To verify our experimental results we performed finite element method (FEM) simulations based on a simple model

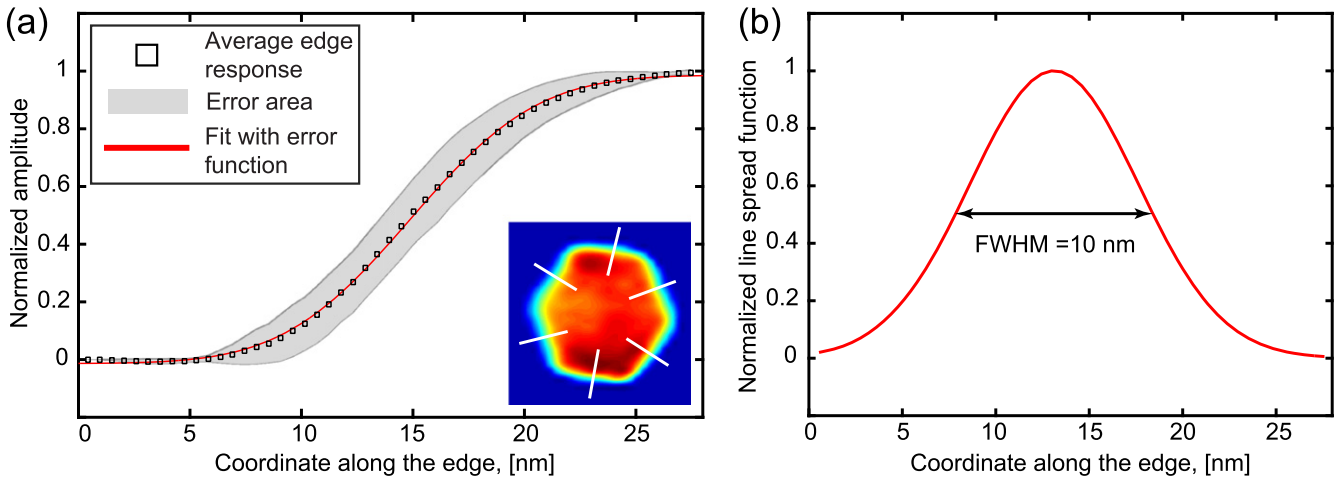

Figure 6. Resolution evaluation (a) an averaged edge scan of six facets of the NW (see inset) with the spread of values for each point (shown by gray area). Data points were fitted by error function. (b) A corresponding line spread function (LSF), as the derivative of the error function. The FWHM of the LSF is equal to 10 nm.

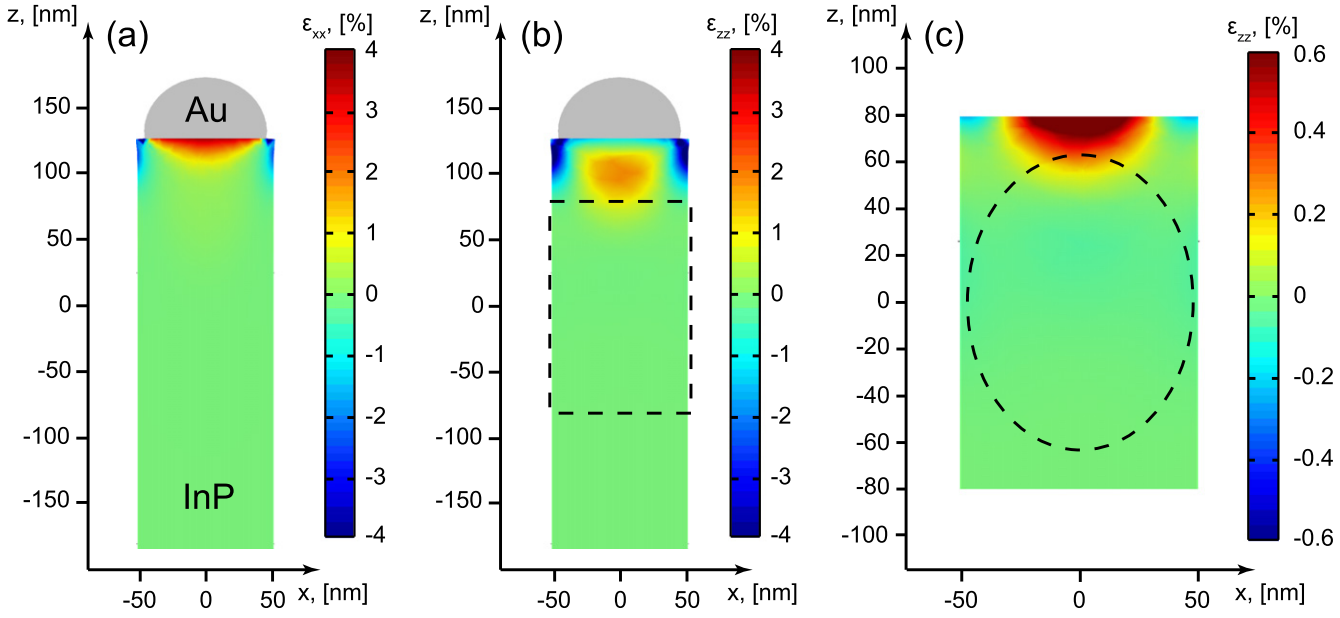

Figure 7. Result of the FEM simulation. The x–z slices at $y = 0$ nm are presented. (a) Distribution of $\varepsilon_{xx}(\mathbf{r})$ strain component. The shape represents deformation of the NW and Au particle. The center of Au particle is located at the $z = 150$ nm. (b) Distribution of $\varepsilon_{zz}(\mathbf{r})$ strain component. The region of the CXDI measurement is shown by dashed rectangle. (c) The region from (b) with the smaller range of $\varepsilon_{zz}(\mathbf{r})$ values. The FWHM of the beam amplitude is shown by the dashed contour.

of the InP NW with the Au particle on the top. Simulations were done within the framework of the linear theory of elasticity. The model consisted of the InP hexagonal shaped NW with dimensions of 100 nm in diameter and 500 nm in length, and a semi-spherical Au particle with diameter of 86 nm, matching the distance between facets of the NW. Epitaxy at the interface between InP and Au was expected to appear due to the minimum mismatch between two unit cells of InP ($d_{10\bar{1}}^{\mathrm{InP}} = 2\sqrt{2}\,a_{\mathrm{InP}}$) and three unit cells of Au ($d_{10\bar{1}}^{\mathrm{Au}} = 3\sqrt{2}\,a_{\mathrm{Au}}$) oriented in [111] direction, where a_{InP} and a_{Au} are the lattice constants of InP and Au (lattice constants of the materials used in the FEM model were $a_{\mathrm{Au}} = 4.0782$ A [39], $a_{\mathrm{InP}} = 5.8687$ A [40]). Misfit strain induced by the lattice mismatch between InP and Au was calculated as

$$\varepsilon_{\mathrm{misfit}} = \varepsilon_{xx} = \varepsilon_{yy} = \frac{d_{10\bar{1}}^{\mathrm{Au}} - d_{10\bar{1}}^{\mathrm{InP}}}{d_{10\bar{1}}^{\mathrm{Au}}}, \tag{8}$$

that resulted in 4% lattice mismatch. This value was applied at the interface between Au and InP for strain components along x and y directions (see for example a 2D slice of the strain component $\varepsilon_{xx}(\mathbf{r})$ distribution in figure 7(a)). The FEM solution was obtained by minimizing the energy of the system via elastic relaxations.

The result of elastic strain relaxation $\varepsilon_{zz}(\mathbf{r})$ is presented in figure 7(b) as a 2D slice at $y = 0$. The interface of two materials is located at $z = 125$ nm. The strain distribution

calculated by the FEM propagates to the region of the CXDI measurement centered at $z = 0$ nm (region of interest is represented by the dashed contour). This area is shown in figure 7(c) with the smaller range of ε_{zz} strain component values. A positive gradient of the ε_{zz} strain component along the z direction has values in the same range as in our measurement (see figure 5(f)) in the region illuminated by the beam (shown by the dashed contour). In order to give a confirmative answer to the question of possible strain distribution at different distances from the Au particle it will be desirable to perform 2D and 3D ptychography measurements of a single NW [41].

6. Conclusions

In summary, 3D reconstruction of the strain distribution in a single free-standing InP NW was performed with a nanofocused beam using the Bragg CXDI technique. We observed a small positive gradient of the $\varepsilon_{zz}(\mathbf{r})$ strain component in the range of $\pm 0.6\%$ in the reconstructed region approximately 150 nm below the Au particle. The quantitative values of the strain component along the [111] direction were obtained by taking into account the reconstructed beam profile from the ptychography measurement. That was an important procedure in the data analysis, that provided us with the reliable information about the strain distribution due to the extended shape of the sample in one-dimension. The spatial resolution in our measurements was determined to be about 10 nm in the direction perpendicular to the facets of the NW. Results of the CXDI measurements were compared with the FEM simulations and show a good agreement with our experimental results.

CXDI in Bragg geometry opens a great opportunities for non-destructive characterization of nano-objects like semiconductor NWs. We believe, that the presented method of 3D Bragg CXDI can improve the understanding of nanostructures functionality by performing studies of 3D strain field distribution under *operando* conditions.

Acknowledgments

This work was supported by European project 280773 'Nanowires for solid state lighting' (NWs4LIGHT) with participating of Lund University, Technical University of Denmark, GLO AB, DESY, and University of Copenhagen and the Virtual Institute VH-VI-403 of the Helmholtz Association. The authors are thankful to E Weckert for fruitful discussions and support, V Kaganer for illuminating discussions, and D Novikov for a careful reading of the manuscript.

References

[1] Qian F, Gradecak S, Li Y, Wen C Y and Lieber C M 2005 *Nano Lett.* **5** 2287–91
[2] Yan R, Gargas D and Yang P 2009 *Nat. Photon.* **3** 569–76
[3] Chen C Y, Zhu G, Hu Y, Yu J W, Song J, Cheng K Y, Peng L H, Chou L J and Wang Z L 2012 *ACS Nano* **6** 5687–92
[4] Wallentin J *et al* 2013 *Science* **339** 1057–60
[5] Krogstrup P, Jø rgensen H I, Heiss M, Demichel O, Holm J V, Aagesen M, Nygard M and Morral A F I 2013 *Nat. Photon.* **7** 306–10
[6] Ju S, Facchetti A, Xuan Y, Liu J, Ishikawa F, Ye P, Zhou C, Marks T J and Janes D B 2007 *Nat. Nanotechnol.* **2** 378–84
[7] Colinge J P *et al* 2010 *Nat. Nanotechnol.* **5** 225–9
[8] Dasgupta N P, Sun J, Liu C, Brittman S, Andrews S C, Lim J, Gao H, Yan R and Yang P 2014 *Adv. Mater.* **26** 2137–84
[9] Novotny C 2007 A study of InP nanowires: growth, material properties, and application in optoelectronics *PhD Thesis* UC San Diego
[10] Montazeri M *et al* 2010 *Nano Lett.* **10** 880–6
[11] Kuhn K J 2011 *Microelectron. Eng.* **88** 1044–9
[12] Conesa-Boj S, Boioli F, Russo-Averchi E, Dunand S, Heiss M, Rüffer D, Wyrsch N, Ballif C, Miglio L and Morral A F I 2014 *Nano Lett.* **14** 1859–64
[13] Larsson M W, Wagner J B, Wallin M, HÅ kansson P, Fröberg L E, Samuelson L and Wallenberg L R 2007 *Nanotechnology* **18** 015504
[14] Chen J, Conache G, Pistol M E, Gray S M, Borgström M T, Xu H, Xu H Q, Samuelson L and Hå kanson U 2010 *Nano Lett.* **10** 1280–6
[15] Hrauda N *et al* 2011 *Nano Lett.* **11** 2875–80
[16] Etzelstorfer T *et al* 2014 *J. Synchrotron Radiat.* **21** 111–8
[17] Franz H *et al* 2006 *Synchrotron Radiat. News* **19** 25–9
[18] Schropp A *et al* 2010 *Appl. Phys. Lett.* **96** 091102
[19] Schropp A, Hoppe R, Patommel J, Samberg D, Seiboth F, Stephan S, Wellenreuther G, Falkenberg G and Schroer C 2012 *Appl. Phys. Lett.* **100** 253112
[20] Döring F *et al* 2013 *Opt. Express* **21** 19311–23
[21] Stankevič T *et al* 2015 *Proc. SPIE* **9592** 95920D
[22] Kriegner D, Persson J, Etzelstorfer T, Jacobsson D, Wallentin J, Wagner J, Deppert K, Borgström M and Stangl J 2013 *Thin Solid Films* **543** 100 – 105
[23] Stankevič T *et al* 2015 *Appl. Phys. Lett.* **107** 103101
[24] Stankevič T *et al* 2015 *J. Appl. Crystallogr.* **48** 344–9
[25] Favre-Nicolin V, Eymery J, Koester R and Gentile P 2009 *Phys. Rev.* B **79** 195401
[26] Pfeifer M A, Williams G J, Vartanyants I A, Harder R and Robinson I K 2006 *Nature* **442** 63–6
[27] Robinson I and Harder R 2009 *Nat. Mater.* **8** 291–8
[28] Vartanyants I and Yefanov O 2015 Coherent x-ray diffraction imaging of nanostructures *X-Ray Diffraction. Modern Experimental Techniques* (Singapore: Pan Stanford) ch 12, pp 341–84
[29] Fienup J R 1982 *Appl. Opt.* **21** 2758–69
[30] Gulden J, Mariager S, Mancuso A, Yefanov O, Baltser J, Krogstrup P, Patommel J, Burghammer M, Feidenhans'l R and Vartanyants I 2011 *Phys. Status Solidi* A **208** 2495–8
[31] Diaz A, Mocuta C, Stangl J, Mandl B, David C, Vila-Comamala J, Chamard V, Metzger T H and Bauer G 2009 *Phys. Rev.* B **79** 125324
[32] Vartanyants I and Robinson I 2001 *J. Phys.: Condens. Matter* **13** 10593
[33] Magnusson M H, Deppert K, Malm J O, Bovin J O and Samuelson L 1999 *Nanostruct. Mater.* **12** 45–8
[34] Kriegner D, Wintersberger E, Kawaguchi K, Wallentin J, Borgström M T and Stangl J 2011 *Nanotechnology* **22** 425704
[35] Schroer C G *et al* 2010 *Nucl. Instrum. Meth.* A **616** 93–7
[36] Muller R A and Buffington A 1974 *J. Opt. Soc. Am.* **64** 1200–10
[37] Dzhigaev D *et al* 2014 *J. Phys.: Conf. Ser.* **499** 012020
[38] Marchesini S, He H, Chapman H N, Hau-Riege S P, Noy A, Howells M R, Weierstall U and Spence J C H 2003 *Phys. Rev.* B **68** 140101

[39] Maeland A and Flanagan T B 1964 *Can. J. Phys.* **42** 2364–6
[40] Levinshtein M, Rumyantsev S and Shur M (ed) 1996 *Handbook Series on Semiconductor Parameters* vol 1 (Singapore: World Scientific)
[41] Dzhigaev D, Stankevič T, Besedin I, Lazarev S, Shabalin A, Strikhanov M N, Feidenhans'l R and Vartanyants I A 2015 *Proc. SPIE* **9592** 95920S